Shear localization behavior in hat-shaped specimen of near-α Ti−6Al−2Zr−1Mo−1V titanium alloy loaded at high strain rate

Yu-xuan DU[1,2], Xin-liang YANG[2], Zu-shu LI[2], Fang HAO[1,3], You-chuan MAO[1,3],
Shao-qiang LI[1], Xiang-hong LIU[1], Yong FENG[1], Zhi-ming YAN[2]

1. Western Superconducting Technologies Co., Ltd., Xi'an 710018, China;
2. WMG, University of Warwick, Coventry CV4 7AL, UK;
3. State Key Laboratory of Solidification Processing, Northwest Polytechnical University, Xi'an 710072, China

Abstract: The microstructure characteristics in early stage shear localization of near-α Ti−6Al−2Zr−1Mo−1V titanium alloy were investigated by split Hopkinson pressure bar (SHPB) tests using hat-shaped specimens. The microstructural evolution and deformation mechanisms of hat-shaped specimens were revealed by electron backscattered diffraction (EBSD) method. It is found that the nucleation and expansion of adiabatic shear band (ASB) are affected by both geometric and structural factors. The increase of dislocation density, structure fragment and temperature rise in the deformation-affected regions provide basic microstructural conditions. In addition to the dislocation slips, the extension twins detected in shear region also play a critical role in microstructural fragmentation due to twin-boundaries effect. Interestingly, the sandwich structure imposes a crucial influence on ASB, which finally becomes a mature wide ASB in the dynamic deformation. However, due to much larger width, the sandwich structure in the middle of shear region is also possible to serve as favorable nucleation sites for crack initiation.
Key words: Ti−6Al−2Zr−1Mo−1V alloy; adiabatic shear band; split Hopkinson pressure bar; hat-shaped specimen; sandwich structure

1 Introduction

The phenomenon of shear localization in high strain rate deformation has attracted significant attention for the impact experiencing occasions since the first recognition of its adiabatic nature by ZENER and HOLLOMON [1] in 1944. The shear strain localized region, i.e., adiabatic shear band (ASB), experiences severe plastic deformation and sharp temperature increasing during such impact deformation. The microstructure in the ASBs was found to be changed dramatically due to the dynamic recovery, recrystallization and phase transformation, which is considered as the origin of the catastrophic failure of metallic materials under dynamic loading [2,3]. Hence, a large number of theoretical and experimental investigations were focused on the formation and microstructural evolution of shear bands [4−10], the criteria for shear band formation [11−13], phase transformation in shear bands [14,15], and the mechanism of recrystallization [16,17].

Among the engineering metallic metals, titanium and its alloys are susceptible to adiabatic shear localization because of their low thermal conductivity and insufficient slip system when experiencing high strain rate plastic deformation [2,6]. Extensive investigations were carried out for the shear localization behavior of

pure titanium [6,18−20] and Ti−6Al−4V titanium alloy [21−25] because of the phase simplicity for the fundamental understanding and wide applications in aircraft frame and jet engine structures, respectively. In the past two decades, the near-α Ti−6Al−2Zr−1Mo−1V titanium alloy, as a moderate strength weldable titanium alloy with advanced strength at elevated temperature, has attracted great attention on its quasi-static performances [26−30]. In order to expand its application to the dynamic loading service, understanding of the shear localization and adiabatic shear band formation of Ti−6Al−2Zr−1Mo−1V titanium alloy is essential for the material selection.

　　Due to the catastrophic characteristics of the mechanical failure in dynamic deformation, it is critical to reveal the mechanisms in the initiation of shear localization. Here, the initiation is defined as the stage from strain hardening to the start of instable softening. A comprehensive study by MEYERS et al [6] classified the dominant factors of shear localization in the α-titanium into the geometrical aspect of strain concentration site and microstructural inhomogeneity. Second-phase particles, dislocation pileups [31], crystallographic orientation of grains [32] may also serve as the initiation sites of strain concentration. LONGÈRE [33] used a unified model to evaluate the roles of thermal softening and dynamic recrystallization (DRX) in ASB initiation. It is shown that for very late DRX onset, ASB initiation is controlled by thermal softening, whereas for very early DRX onset, ASB initiation is (mainly) controlled by DRX softening. GUO et al [34] investigated adiabatic shear behavior of pure titanium with high-speed photography and infrared temperature measurement and proposed that the time sequence is stress collapse, ASB initiation, temperature rise and crack formation. With the existence of β-Ti (bcc) phase between the α-titanium laths, the underlying mechanism of shear band initiation may vary due to the phase inhomogeneity and the difference of slip activation mode between the hcp α-Ti and bcc β-Ti phases.

　　This work focuses on the microstructure characteristics of Ti−6Al−2Zr−1Mo−1V hat-shaped specimen [35,36] in the early stage of SHPB impact loading. An interesting phenomenon of shear band bifurcation is found in the shear region of the hat-shaped specimen. Furthermore, a special sandwich structure is also found. The micro-structure characteristics and their influence on ASB initiation and formation are revealed and the fundamental understanding of the initiation of shear localization of the Ti−6Al−2Zr−1Mo−1V titanium alloy is provided.

2 Experimental

　　The as-received Ti−6Al−2Zr−1Mo−1V alloy is in the form of as-annealed billets with a diameter of 400 mm. The β transus temperature by the metallographic measurement is confirmed to be ~1263 K. The initial microstructure of the as-received Ti−6Al−2Zr−1Mo−1V alloy billet is displayed in Fig. 1, from which the volume fraction of equiaxed primary α phase with average size of (18.0±2.0) μm is confirmed to be (50±5)%; while coalesced secondary α-Ti phases are with a thickness of (2.0±0.5) μm. In addition, the volume fraction of β-Ti phase in the as-received Ti−6Al−2Zr−1Mo−1V alloy is 5.6%. The (0001) pole figure (see Fig. 1(b)) of α-Ti phase in the as-received
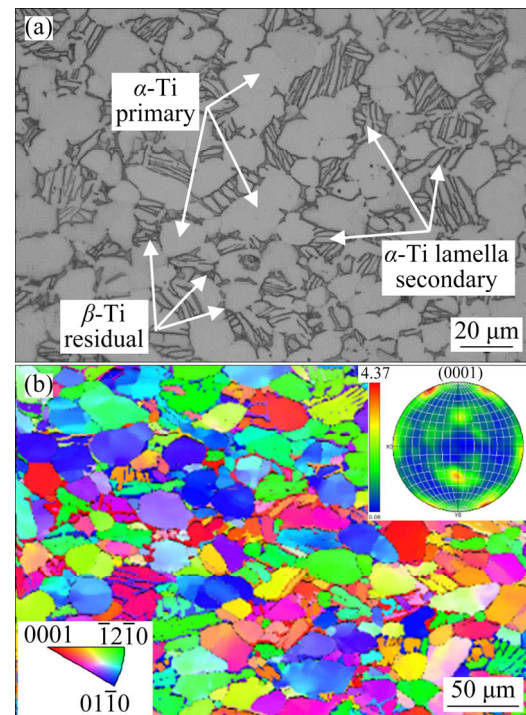

Fig. 1 Microstructure of as-received Ti−6Al−2Zr−1Mo−1V alloy sample from longitudinal section of forged billet: (a) Optical image of etched sample; (b) Inverse pole figure (IPF) map of α-Ti phase and its corresponding (0001) pole figure

Ti−6Al−2Zr−1Mo−1V material shows a weak forged texture. The optical observation and EBSD image indicate that microstructures in the as-received material are homogeneous.

Slices with a thickness of 15 mm were sectioned, then cylindrical pieces (12 mm × 12 mm) were cut for hat-shaped specimens prepared using electrical discharge process along the radial direction. The schematic diagram of hat-shaped specimen is shown in Fig. 2(a). With such typical geometric feature, shear strain can be intensely favored in the region marked by red lines in Fig. 2(a).

Dynamic compression tests were conducted at ambient temperature (~25 °C) using the split Hopkinson pressure bar (SHPB) system. The set-up of SHPB system is illustrated in Fig. 3, in which the hat-shaped specimen is placed between the incident bar and transmitted bar. An impact pulse is generated by a striker bar driven by a gas gun. The lengths of striker bar, incident bar and transmitted

bar, which are made of C350 maraging steel, are 0.2, 1.0 and 1.0 m, respectively. The diameter of these bars is 14.5 mm. The average displacement velocity of the hat-shaped specimens in SHPB tests is 3 m/s. Dynamic compression tests are repeated twice to ensure the reliability of the data.

After that, the specimen is etched in a solution of 8% tetrafluoroboric acid for 90 s. Macroscopic images are taken on a Nikon SMZ18 Stereo microscope system. Metallographic examination is carried out on a Nikon Eclipse LV150N optical microscope. The fracture morphology is examined on a Hitachi TM3030 plus tungsten source scanning electron microscope (SEM). Electron backscattered diffraction analysis is processed on a JEOL 7800F field emission SEM equipped with Symmetry[TM] (Oxford instrument). The accelerating voltage is 20 kV, probe current is 14 nA, scanning speed is 815 Hz, and scanning step sizes of 0.1, 0.15, 0.2 and 1 μm are used for areas of 0.06, 0.16, 0.25 and 2.88 mm^2, respectively.
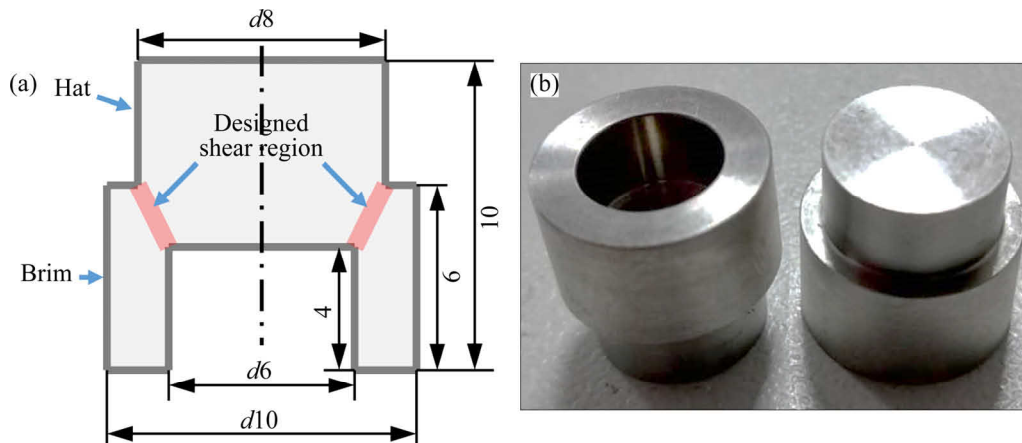

Fig. 2 Hat-shaped specimen for controlled shear deformation under impact experiment: (a) Dimensions of hat-shaped specimen with designed shear region by geometrical assistance (unit: mm); (b) Photo of Ti−6Al−2Zr−1Mo−1V alloy sample with hat-shaped layout
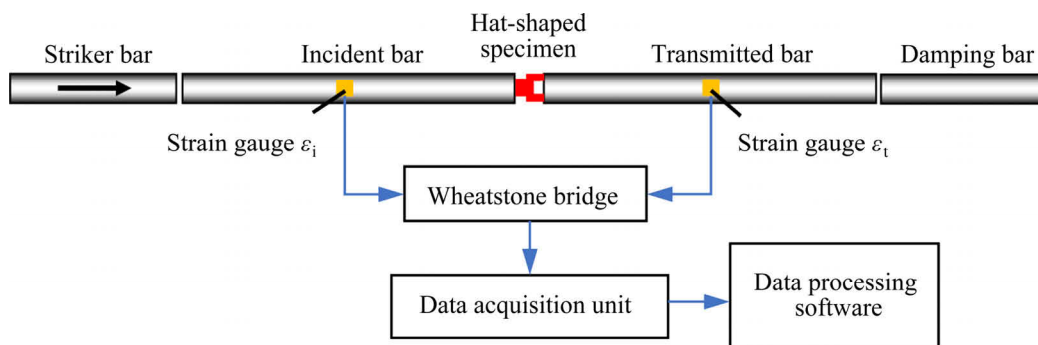

Fig. 3 Schematic illustration of split Hopkinson pressure bar set-up (ε_i is strain signal of incident pulse, ε_t is strain signal of transmitted pulse, and average displacement velocity of hat-shaped specimens is 3 m/s)

3 Mechanical response and micro-structures

3.1 Mechanical response at high strain rate

In SHPB test, the force applied to the hat-shaped Ti−6Al−2Zr−1Mo−1V alloy specimen can be calculated from the signals collected by the strain gauges on the incident and transmitted bars. According to PEIRS et al [35], the applied axial force F and the top-to-bottom surface displacement of the sample Δu can be calculated by the following equations:

$$F = E_0 A_b \varepsilon_t \tag{1}$$

$$\Delta u = C_0 \int_0^t \varepsilon_r \mathrm{d}t \tag{2}$$

where E_0 and C_0 are the elastic modulus and elastic wave speed in Hopkinson bar, respectively; A_b is the area of cross-section in transmitted bar; ε_r and ε_t represent the strain signals of reflected and transmitted pulse on the Hopkinson bars, respectively.

Figure 4(a) shows the force−displacement curve of the hat-shaped Ti−6Al−2Zr−1Mo−1V alloy specimen in the SHPB test. From the curve, it is found that the plastic deformation experiences three stages. In the first stage ($A{\rightarrow}B$), the force increases with increasing displacement due to the strain hardening. The peak force reaches 66142 N at the displacement of 0.157 mm. In the last stage ($C{\rightarrow}D$), the force drops sharply because of the dynamic recrystallization (DRX) caused by predominant thermal-softening effect. The middle stage ($B{\rightarrow}C$) shows mild decreasing tendency in force. This indicates that more deformation is needed to overcome the energy barrier of the initiation and propagation of ASB before ASB is mature. Similar mechanical behavior was reported by KUANG et al [37] in the study of dynamic response of a forged and vacuum annealed commercially pure titanium material in the SHPB test.

Figure 4(b) shows the photo of the hat-shaped specimen after SHPB test. During the SHPB test, the hat-portion of the sample is pressed into the brim-portion, and the gap between the two parts appears as a black line from the top of the sample, which is called "sunk line" in this work for the convenience of description. It can be clearly seen that inhomogeneous deformation was induced due to the typical layout of specimen. The left side of the hat-portion is pressed more deeply into the brim-portion than the other side. The sunk line (marked by red line) indicates that in this region compressive deformation is severer than that in the rest region (about 1/4 circle). In the following chapter, this phenomenon will be discussed in detail.

3.2 Microstructures in shear region

Figure 5 exhibits the overall microstructure of the specimen. The shear region highlighted with the blue and orange rectangles represent low strain loading side and high strain loading side, respectively. On the low strain loading side, the crack initiation is observed at the upper and lower corner positions. Along the shear region (indicated by red dashed lines) of high strain loading side, the typical microstructure is observed, which starts from the two corners and expands towards the middle of shear region. Similar results are observed in other studies [6,38,39], in which it is believed that geometric condition favored such phenomenon. Based on the development of shear localization and
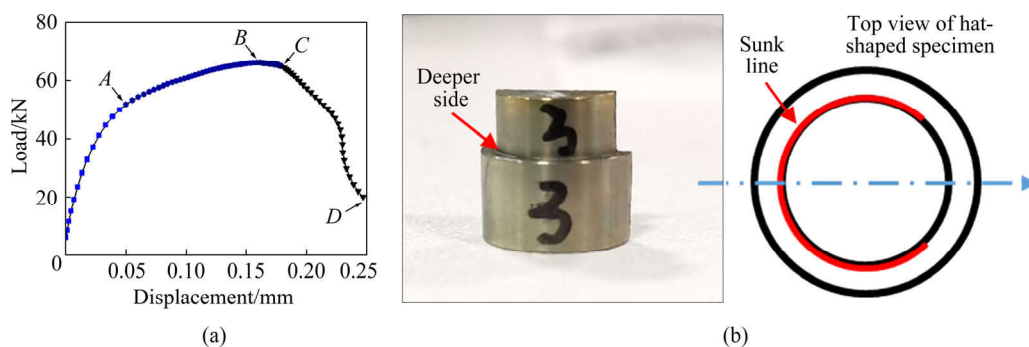

(a)   (b)

Fig. 4 Load−displacement curve of Ti−6Al−2Zr−1Mo−1V alloy specimen under SHPB test with average displacement velocity of 3 m/s (a) and inhomogeneous deformation along intersecting circumference of hat-portion and brim-portion and schematic selection of longitudinal section (b)

ASBs formation, four areas are identified as localized deformation area (Area 1), ASB initiation area (Area 2), continuous ASB area (Area 3) and mature ASB area (Area 4), respectively.

Figure 6 shows the EBSD maps of shear regions in the Ti−6Al−2Zr−1Mo−1V alloy specimen. The band contrast (BC) map is used to identify the position of severely localized ASBs by filtering the map with grey-level≤30.

In combination with Fig. 5, it is confirmed that the black band in Fig. 6(a_1) represents ASBs. The black strips on both corners of low strain shear region (Fig. 6(b_1)) indicate that ASBs have initiated

and propagated into middle of shear region to form integrated ASBs. Figures 6(a_2, b_2) display the KAM maps of the high and low strain-loading areas of specimens, respectively. To better understand the misorientation distribution, it is assumed that microstructure with misorientation larger than 2° is classified as deformation-affected region (indicated by white dashed lines); the rest part of the shear region is regarded as the parent microstructure (with misorientation <2°). Therefore, the shear region of hat-shaped sample contains three main regions: ASBs, deformation-affected region and parent structure. In the IPF maps with the mean
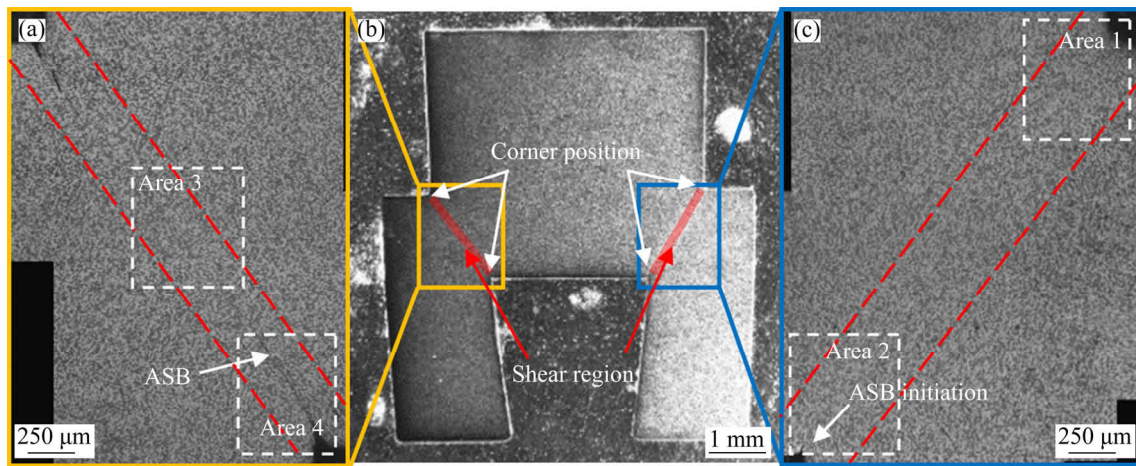

Fig. 5 Overview of longitudinal cross-section of hat-shaped Ti−6Al−2Zr−1Mo−1V alloy specimen presenting two distinct areas with different shear strains: (a) OM image of high strain shear region with ASB formation and micro-cracks; (b) Cross-section of hat-shaped specimen; (c) OM image of low strain shear region with ASB initiation in corner
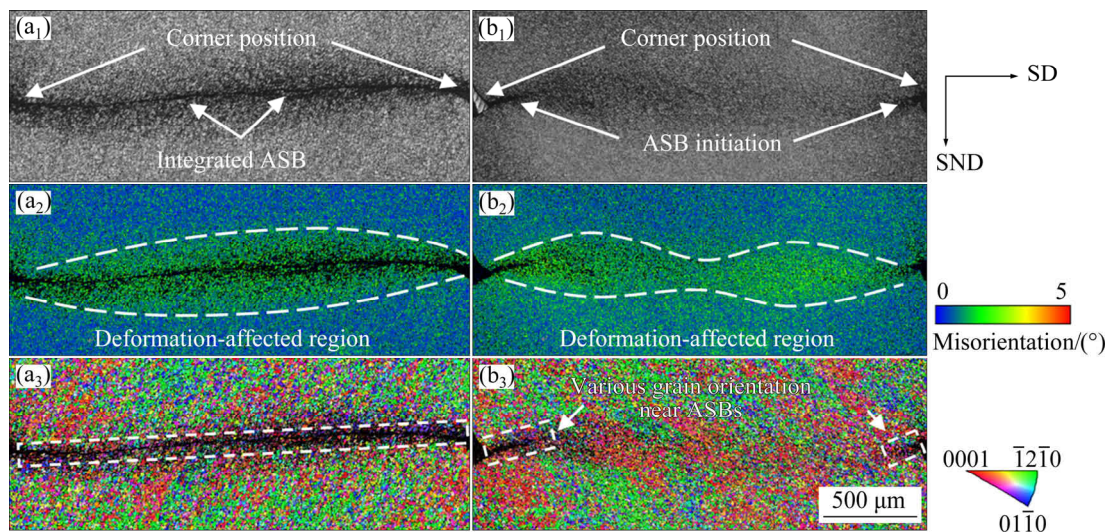

Fig. 6 EBSD maps of shear regions with different strains loading in Ti−6Al−2Zr−1Mo−1V alloy specimen in Fig. 5: (a_1, a_2, a_3) Band contrast (BC), kernel average misorientation (KAM) and inverse pole figure (IPF) maps of high strain shear region, respectively; (b_1, b_2, b_3) BC, KAM and IPF maps of low strain shear region, respectively (Sample coordinate is indicated with shear direction (SD) and shear normal direction (SND))

angular deviation of 0.71 (Figs. 6(a$_3$, b$_3$)), the grain misorientation in the deformation-affected region suggests the localized nature of the shear deformation applied on the Ti−6Al−2Zr−1Mo−1V alloy under high strain rate.

3.3 Deformation behaviors

3.3.1 Under low shear strain condition

Figure 7 shows the enlarged microstructures of Area 1 in Fig. 5. From the optical image in Fig. 7(a), a crack is nucleated and leads to a serrated shape of the corner edge. From the BC map in Fig. 7(b), the black feature (grey-level ≤30) with severely distorted crystal lattice suggests that local deformation of α-Ti grains initiates from the tip of

the sample corner and locally extends along the shear direction. The $\{10\bar{1}2\}$ extension twins with width of (1.0±0.5) μm are the dominant twinning system in the deformation-affected region. As we all know that twining activation is known to be one of the major mechanisms to accommodate the shear strain in the impact deformation of the Ti−6Al−2Zr−1Mo−1V alloy. Furthermore, the IPF (Fig. 7(c)) and geometrically necessary dislocation (GND) maps (Fig. 7(d)) show the evidence of microstructure subdivision: the subgrain structure in the primary α-Ti grains with large misorientation, the small α-Ti grains with various orientations compared to their parent structure, and the high density GNDs concentrating locally near the
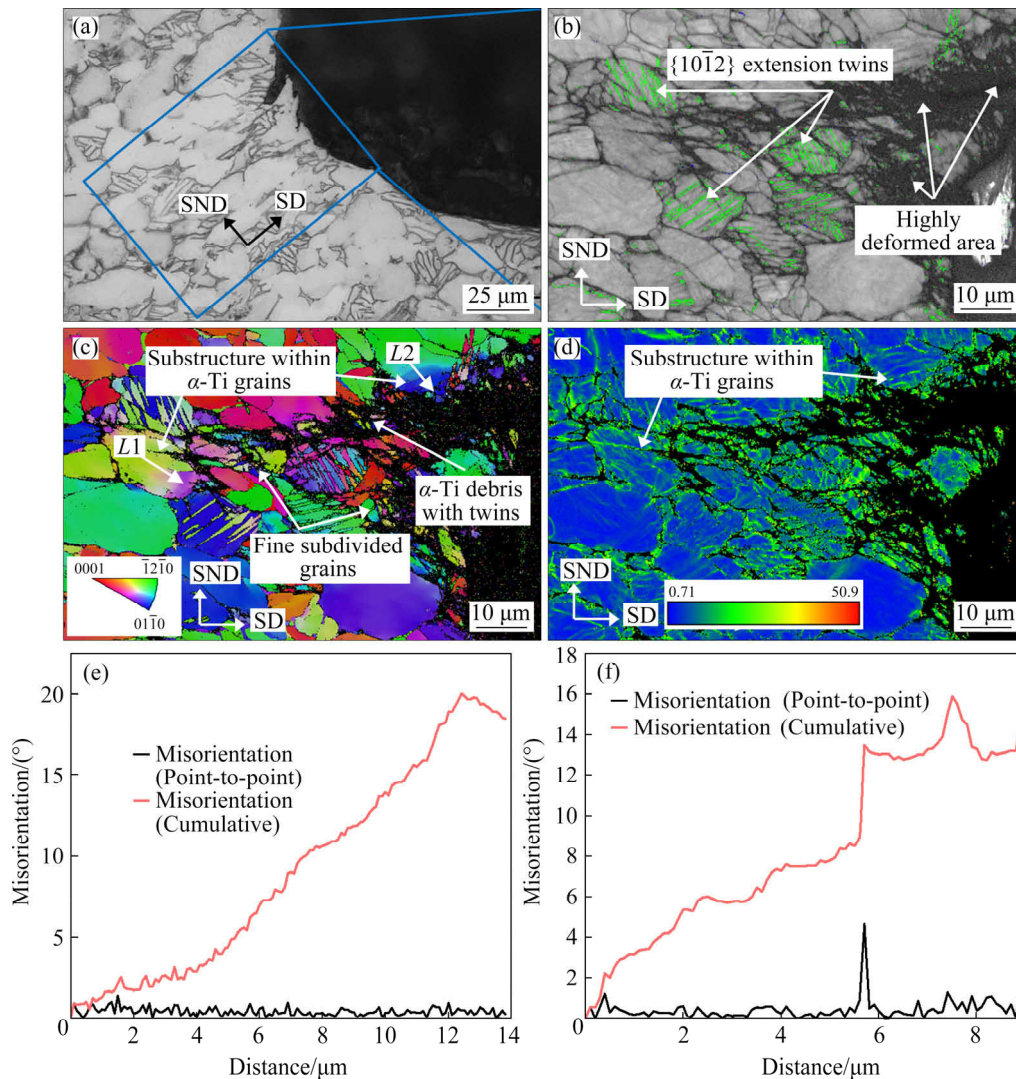

Fig. 7 Microstructures (a−d) and misorientation distribution lines (e, f) of Ti−6Al−2Zr−1Mo−1V alloy sample of Area 1 in Fig. 5: (a) Optical microstructure; (b) BC map (green lines for $\{10\bar{1}2\}$ extension twins, red lines for $\{11\bar{2}1\}$ extension twins, and blue lines for $\{11\bar{2}2\}$ contraction twins); (c) IPF map; (d) Geometrically necessary dislocation (GND) map (color-scale in (e) is lg ρ_{GND}, where ρ_{GND} is GND density in m^{-2}); (e, f) Misorientation distribution along $L1$ (e) and $L2$ (f) labelled in Fig. 7(c), respectively

severely deformed location. These subgrain boundaries are formed as a result of GND concentration (Fig. 7(d)). The misorientation profiles along Lines $L1$ and $L2$ in Fig. 7(c) are presented in Figs. 7(e) and (f), respectively. It is obviously seen that the misorientation profiles in Figs. 7(e) and (f) exceed 15°, which is defined as the boundary between high and low grain boundary angles. Note that the misorientation induced by pure dislocation effect is usually lower than 15°. This fact indicates that α-Ti grain has been subdivided into small size structure in Area 1.

Figure 8 shows the enlarged microstructures of

the Area 2 in Fig. 5. Compared to the initiation area of ASBs in Fig. 7, more deformation features are obtained in this region. As shown in Fig. 8(a), two narrow ASBs marked with ASB 1 and ASB 2 start from the corner position and develop towards the middle of the shear region. The average widths of these two ASBs are (0.6±0.1) μm for ASB 1 and (0.8±0.1) μm for ASB 2. Correspondingly, the areas occupied by black strip features in Figs. 8(b, c) can be confirmed as the position where ASB initiates. In the meantime, these results exhibit the propagation path of the early stage ASB structure. ASB 1 is close to the vertical direction, whereas
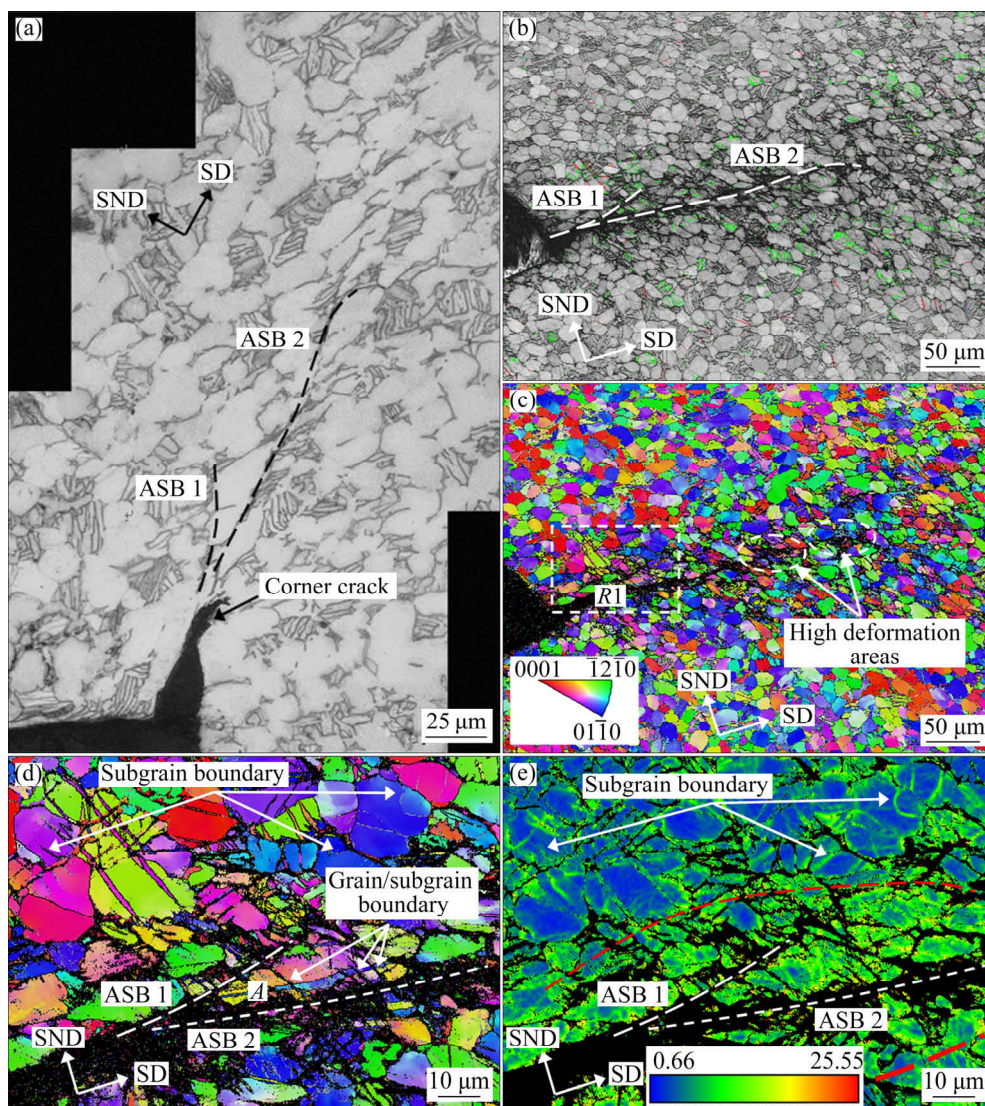

Fig. 8 Microstructures of Area 2 in Fig. 5 (corner position of shear region on low strain loading side of Ti−6Al−2Zr−1Mo−1V alloy with visible ASBs): (a) Optical microstructure of shear region; (b) BC map of same region with highlighted twin boundaries (green lines for $\{10\bar{1}2\}$ extension twins, red lines for $\{11\bar{2}1\}$ extension twins, and blue lines for $\{11\bar{2}2\}$ contraction twins); (c) IPF map of shear region (Two individual ASBs are indicated with dash lines); (d) IPF map of Region $R1$ in (c); (e) GND map of region $R1$ in (c) demonstrating sandwich structure composed of ASBs and between α-Ti grains

ASB 2 is along the shear direction. As shown in the tip of ASB 2 (Figs. 8(b, c)), the high deformation areas are introduced by the local variation of grain orientation, morphology, and crystal structure of α/β-Ti phases. This implies that the microstructural factors influence the propagation of ASB structure and further lead to an intermittent manner of shear localization. In Fig. 8(b), the twin boundaries of $\{10\bar{1}2\}$ extension twins are suggested to be the major twin system in the area near the ASB location and the volume of $\{11\bar{2}1\}$ twin, marked with red lines, is increased compared to that in the ASB initiation area in Fig. 7(b). In order to study the detailed microstructure in the ASB starting area, Region $R1$ in Fig. 8(c) is further analyzed. Similar to the area represented in Figs. 7(c, d), subgrain boundaries composed of concentrated GNDs are observed in the starting area of ASB structure (Region $R1$). It is clearly seen that the distribution pattern of GNDs is closely related with distance to shear band region. High density of GNDs is concentrated in the area adjacent to shear band, especially in Region A in Fig. 8(d). However, with increasing distance, the density of GNDs decreases monotonously. In Region A, large misorientation

spreads within single α-Ti grain, and grain/subgrain boundaries are nearly perpendicular to the shear direction, which contribute to the fragmentation of α-Ti phase in Area A in Fig. 8(d). The sandwich structure is composed of two adjacent narrow ASBs and the region between them (see Fig. 8(e)). With the proceeding of the dynamic loading, the shear deformation tends to be localized in this sandwich structure due to both microstructural and geometric factors.

3.3.2 Under high shear strain condition

Figure 9 shows the enlarged microstructures of Area 3 in Fig. 5, which is in the middle area of the shear region on the high strain loading side. In the optical microstructure in Fig. 9(a), the continuous ASBs cross the middle area of the shear region. The average width of these ASBs is (0.7 ± 0.2) μm. Bifurcation of ASB is observed in Fig. 9(b), and such specific structure is catalogued into primary and secondary bifurcations by the length and width of the ASBs, respectively. As a common feature of ballistic impacting in titanium [23], bifurcation behavior is attributed to the deformation incongruity between the partial recrystallized structures and surrounding completely recrystallized equiaxed
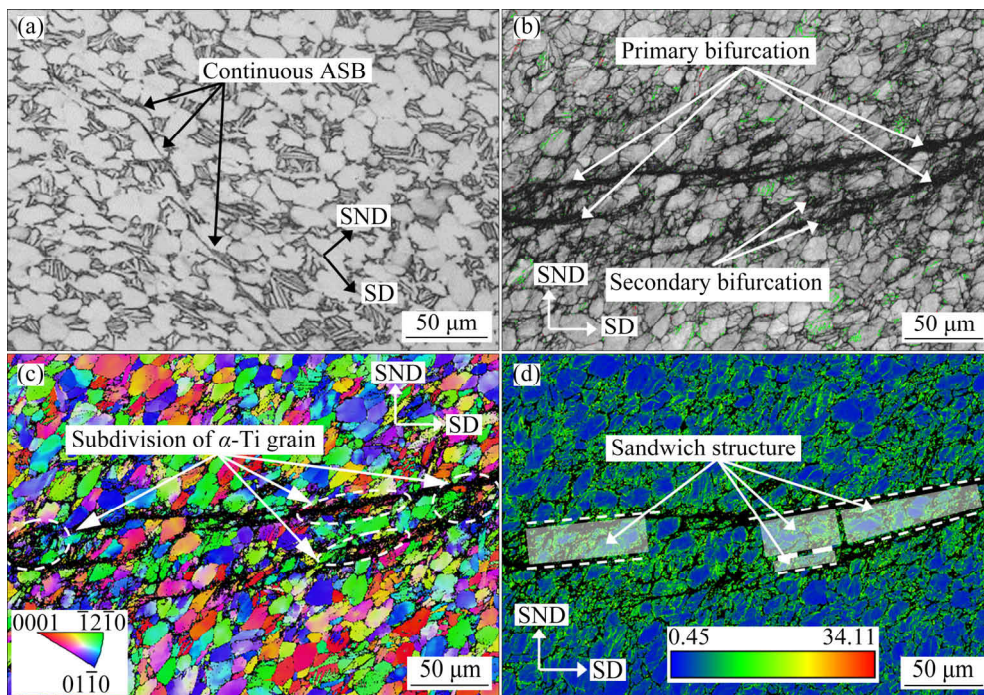

Fig. 9 Microstructures of Area 3 in Fig. 5 (middle area of shear region on high strain loading side of Ti−6Al−2Zr−1Mo−1V alloy with continuous ASB structures): (a) Optical microstructure; (b) BC map showing twinning behavior near ASBs (green lines for $\{10\bar{1}2\}$ extension twins, red lines for $\{11\bar{2}1\}$ extension twins, and blue lines for $\{11\bar{2}2\}$ contraction twins) and bifurcation of ASBs; (c) IPF map presenting microstructure subdivision in mature ASBs area; (d) GND map demonstrating sandwich structure composed of ASBs and between α-Ti grains

grains. In present work, it is known from Fig. 6(a_2) that the deformation-affected region becomes wider in the middle area of shear region, which offers more potential propagating routes for ASB to passing through. In consequence, the bifurcation of ASBs presented here represents the multiple propagating path of ASBs. From IPF map in Fig. 9(c), the subdivision of α-Ti grains is observed along the ASBs by analyzing the difference of crystallographic orientation. Besides, the similar sandwich structures composed of two parallel primary and/or secondary ASBs and the region between them are specified in Fig. 9(d).

Figure 10 shows the enlarged microstructure of Area 4 in Fig. 5. The width of ASBs in this area is (5.6±0.2) μm. As displayed in Fig. 10(a), lamellar structure of significantly stretched α-Ti phases is observed within the ASB. Micro-crack appears along the ASB with further development of mature ASB. The severe deformation has consumed primary α-Ti phase and/or residual β-Ti phase to form elongated lamellar structure for the strain accommodation. Due to the severe deformation, the micro-crack develops to release the excessive strain until the mechanical failure occurs. Besides the corner edge, some micro-cracks also nucleate in the ASBs, as shown in Fig. 10(a). The random distribution of ASB nucleation site is maybe attributed to the hot spots that have been observed in mature ASBs of other metallic materials [40,41]. Furthermore, the crack surface is not smooth, but has a wavy morphology. The hot spots are formed in grains with severe deformation. These grains usually reorientate to accommodate the localized deformation (see Fig. 7). Hence, the initial orientation of micro-cracks originated from these hot spots does not match the direction of the shear band. These micro-cracks rotate and are linked to form larger cracks with wavy surface as the localized deformation progresses. Similar phenomena have also been observed in Ti−6Al−4V alloy hat-shaped specimens during dynamic loading [35,36]. The sharp boundaries between ASB and parent microstructure indicate that the shear strain has strongly localized after onset of instable softening. The extension twinning marked by green lines is distributed mainly near the crack as shown in Fig. 10(b). With increasing shear strain, the density of extension twinning increases monotonously.
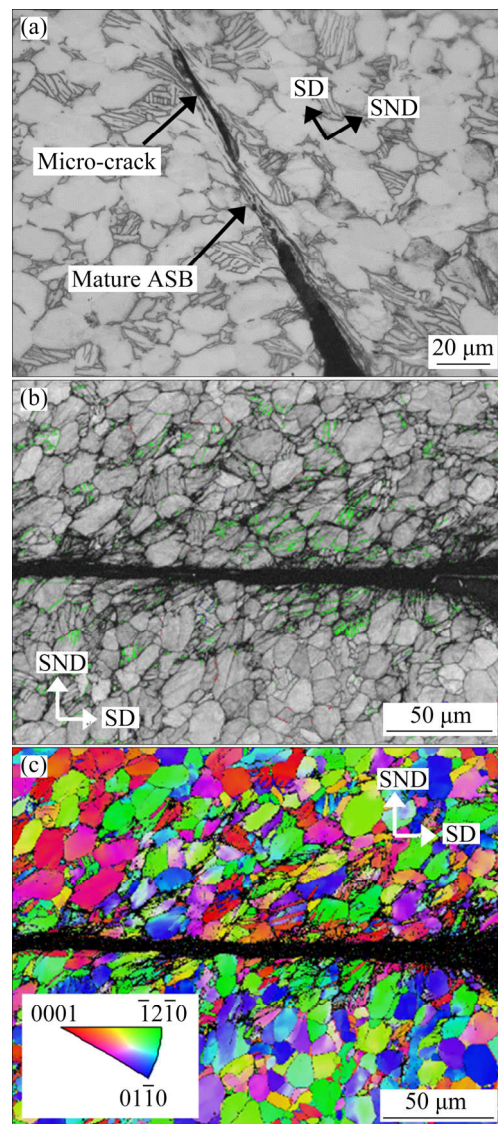

Fig. 10 Microstructures of Area 4 in Fig. 5 (corner position of shear region on high strain loading side of Ti−6Al−2Zr−1Mo−1V alloy with mature ASBs): (a) Optical microstructure revealing mature ASBs and micro-crack nearby; (b) BC map (green lines for $\{10\bar{1}2\}$ extension twins, red lines for $\{11\bar{2}1\}$ extension twins, and blue lines for $\{11\bar{2}2\}$ contraction twins); (c) IPF map

4 Discussion

4.1 Fragmentation of microstructure

The formation of ASB from the beginning of plastic deformation is a continuous process in which shear deformation is localized significantly with the proceeding of deformation loading. Along with it, the microstructure is also subdivided dynamically, which in turn influences the formation and evolution of the ASBs.

Due to the geometric characteristics of the hat-shaped specimen, the plastic deformation is designed to concentrate in the shear region as shown in Fig. 5. The dislocation density increases in this region with the deformation heat generated, which assists the shear localization and initiation of ASBs. Due to the rotation of the crystal orientation, α-Ti grains with favorable orientation for the dislocation slip and/or twinning firstly accommodate the plastic deformation applied on the sample, which leads to the local dislocation concentration and formation of substructure in the primary α-Ti grains accordingly. The micro-scale inhomogeneity of impact deformation results in large misorientation in the primary α-Ti grain, as shown in Figs. 7(e) and (f). The dislocation slips are intensely activated due to the localized shear strain, thus dislocations are twisted and tangled, causing the dislocation cells or walls [16,42]. Therefore, from the macro observation (EBSD), grain shows different colors even in a single block. It is believed that the misorientation in a single grain is attributed to the accumulation of dislocations. The dislocation walls act as the interface between sub-microstructures and matrix. With further increasing localized shear strain, more dislocations are accumulated, which dramatically increases the localized stress field and strain filed. Once the trigger stress is achieved, grains collapse by these dislocation walls, thus causing fragmentation. In addition, deformation twins are also detected after dynamic loading. In fact, twins play a role in fragmentation as well. Even though multiple literatures [43,44] about the transformation induced plasticity (TRIP) effect were reported, if we focus

on severe deformation under high strain rate, something unexpected occurs. It is known that twin boundary is the critical factor that can essentially strengthen materials, in which the dislocation piles up at twin boundaries. Obviously, with further deformation, more dislocations are trapped until collapse, which causes microstructural fragmentation. Thus, it is clear that twins are double-side sword in materials.

4.2 Development of multi-ASBs in early stage of shear deformation

The initiation of multiple ASBs observed in Area 2 with visible ASBs (Fig. 8) has been reported in the metallic materials, such as explosive collapse of a thick-walled cylinder (TWC) [31,32] and ballistic impact test [23,45].

The formation of multiple ASBs in the corner position is schematically illustrated in Fig. 11. At the starting shear strain (γ_{s0}), the bottom surface of hat-portion moves down under the imposed force, so the initial shear direction of ASB is in accordance with the direction of imposed force. The 90° corner position is the favorable site to initiate the first ASB (ASB 1) formation. With further increasing shear strain to γ_{s1}, bottom of hat-portion moves out of stress-imposed region. A sharp angle is formed between the bottom of hat-portion and inside wall of brim, which becomes a new site for stress concentration. Since the plastic deformation has started, shear direction is tilted to link the two corners of shear region, which gradually moves away from force imposing direction. Thus, the deformation-affected region is able to offer an easy propagating route for adiabatic shear localization.
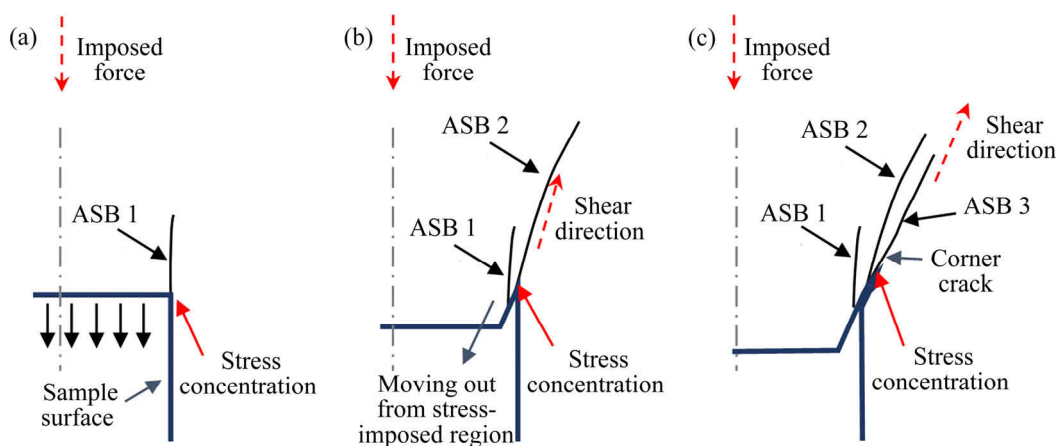

Fig. 11 Schematic illustration of multiple ASBs formation with increase of strain level: (a) Strain γ_{s0}; (b) Strain γ_{s1}; (c) Strain γ_{s2} ($\gamma_{s0} < \gamma_{s1} < \gamma_{s2}$, the shear direction tilts away from constant loading direction)

Consequently, new ASB nucleates and propagates along the shear direction (ASB 2). With increasing strain (γ_{s2}), further tilting of the shear direction alters the local stress condition for new ASB formation before the crossover ASB dominates the adiabatic shear localization (ASB 3 and more). Multiple ASBs formation appears in the early stage of adiabatic shear localization due to various shear directions in a geometry-dominant period. With further microstructure evolution in the shear region, both geometrical factor and microstructural factor affect the formation of single mature ASB.

4.3 Formation of mature ASB from sandwich structure

The feature of the continuous ASB in Fig. 9 indicates the intermediate stage of ASB evolution with increasing strain. Note that the sandwich structure has been observed, we will discuss, in the following, the relationships between formation of mature ASBs and this typical structure in detail.

A schematic illustration of the formation mechanism of ASB from sandwich structure is shown in Fig. 12. In the initial stage of plastic deformation, the deformation-affected regions are formed in relatively large portion of specimen. The inhomogeneous deformation within the affected region leads to the shear localization in some local microstructural favorable positions. At the positions where shear strain is geometrically and micro-structurally satisfied, such as the corners of shear region in the hat-shaped specimen, ASBs are initiated. From Figs. 8(d) and (e), it is known that the shear strain in the region between ASB 1 and ABS 2 is higher than that out of ASBs. Therefore, with increasing strain, local temperature increases

in this region due to the deformation heat caused by friction and adiabatic nature of impact deformation.

The temperature in the shear band can be calculated as follows [46]:

$$T = \frac{\beta W_{\mathrm{P}}}{c_V \rho} + T_0 \tag{3}$$

where β is the heat-converting factor (0.9) that represents the fraction of plastic energy converting to heat [47,48], ρ is the mass density of Ti−6Al−2Zr−1Mo−1V titanium alloy (4530 kg/m^3), c_V is the heat capacity (580 J/K), T_0 is the ambient temperature (298 K) when implementing SHPB test, and W_{P} is the specific plastic work. The relevant material properties are acquired from the database of MeltFlow software [49]. According to the equation, the local temperature rise of Ti−6Al−2Zr−1Mo−1V alloy under SHPB test can reach up to 949 K, which is ~$0.48T_{\mathrm{m}}$ (T_{m} is the melting point of Ti−6Al−2Zr−1Mo−1V alloy (1990 K)).

According to the subgrain rotation dynamic recrystallization model [31], ASBs are generated in metallic materials through the following four steps: (I) dislocations proliferate and distribute randomly during the initial stage of deformation; (II) dislocations rearrange to form elongated dislocation cells, known as the dynamic recovery; (III) elongated subgrains are generated from the dislocation cells as the deformation continues; (IV) elongated subgrains dissolve and rotate into equiaxed recrystallized micrograins. This is consistent with our observations. Deformation of materials at high strain rate is usually considered as an adiabatic process, which accompanies with a continuous rise in temperature. The significant increase in temperature causes the thermal softening
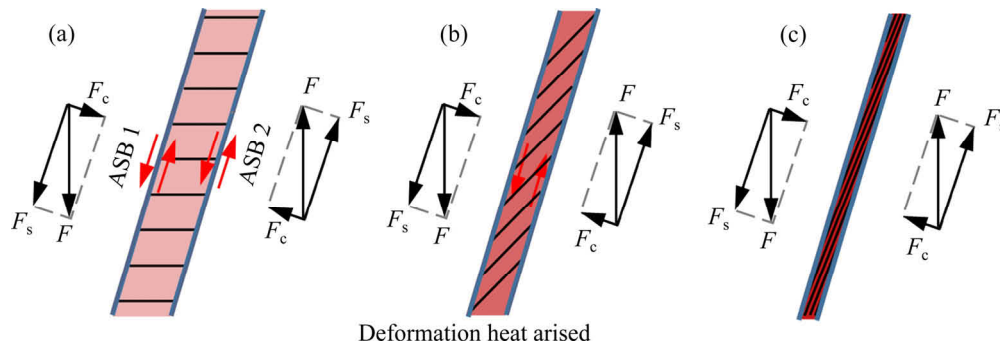

Deformation heat arised

Fig. 12 Schematic diagrams of formation of ASB from sandwich structure (saturation of red color represents local temperature during shear deformation; F represents imposed force, F_s is shear component of F, and F_c is compression component of F): (a) Shear deformation of ASBs and neighboring regions; (b) Shear deformation of region between ASBs with localized deformation; (c) Formation of mature ASB

effect. The higher softening effect is expected to offset the strain hardening, while the region out of ASBs is lack of such effect. With the high temperature, the high order slip may be activated because of the reduced critical resolved shear stress (CRSS) [50−52] caused by adiabatic heat rise (Fig. 12(b)). These evolutions caused by thermal softening facilitate various stages of the ASB formation process, such as dislocations proliferation in Stage I, the formation of dislocation cells or walls in Stage II and the formation of recrystallized micrograins in Stage IV. As a consequence of positive feedback, more deformation heat is generated locally, which further enables more deformation accommodation. Hence, the shear strain is highly concentrated in the region between ASBs. Under the compressive component from the imposed force shown in Fig. 12(c), the width of sandwich structure is reduced with increasing strain and mature ASB is formed in the end.

GRADY and KIPP [8,53,54] investigated the energy dissipation in the adiabatic shear band process and proposed Eq. (4) to calculate the width of adiabatic shear band.

$$a_0 = \left[9\rho^3 C^2 \chi^3 \Big/ \left(\tau_b^3 (\partial \tau / \partial \theta)^2 \dot{\gamma} \right) \right]^{1/4} \tag{4}$$

where C is the specific heat capacity (580 J/(kg·K)), χ is the thermal diffusivity (5.56×10^{-6} m^2/s), τ_b is the flow stress, $\partial \tau / \partial \theta$ is the thermal softening coefficient (595 kPa/K), and $\dot{\gamma}$ is the shear strain rate. The $\partial \tau / \partial \theta$ is from the work of SHAHAN and TAHERI [20] and the material parameters are collected from the database of MeltFlow software [49].

The calculated width of adiabatic shear band is 1.44 μm, which is consistent with ASB width in the middle area of shear regions as shown in Fig. 13. However, the mature ASB width (~5.6 μm) is higher than the calculated results, which may be due to the involvement of microstructural factor, which is neglected in the above equation.

4.4 Shear localization behavior in Ti−6Al−2Zr− 1Mo−1V alloy during SHPB test

As exhibited in Fig. 4, the load−displacement curve of Ti−6Al−2Zr−1Mo−1V alloy under SHPB test is composed of three stages. During the first strain hardening stage, the plastic deformation is concentrated in the shear region of the samples.
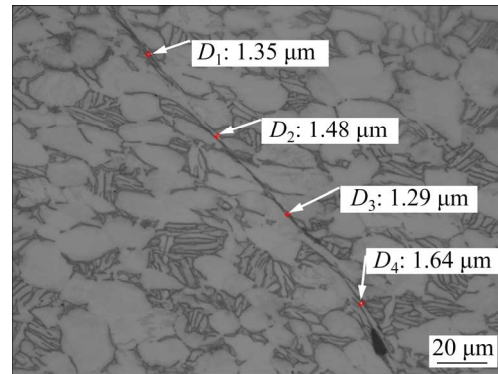

Fig. 13 Metallographic image in ASB located in middle of shear region

According to results in Ref. [39] on localization behavior of stainless steel hat-shaped specimen during SHPB test, the flow stress reaches peak value when the deformation-affected regions from two corner positions contact each other and go to merge into one. Due to the geometrical advantage of corner position in shear region, it is the preferred nucleation site of ASBs. The variation of the corner shape, viscoplastic flow of material from the force-imposed region and tilting of local shear direction, enables the initiation of multiple ASBs, and the sandwich structure is formed. In term of the ASB propagation, the intermittent high deformation areas in the ASB developing region discussed in Section 4.1 offers potential propagating routes of shear localization. From the analysis above, lack of available slip system α-Ti grains results in limited mechanism to accommodate the imposed shear deformation. Therefore, it requires higher stored energy to promote the microstructure evolution, which explains the slow force decline slowly after reaching the peak value. With further increasing strain, sandwich structure in the bottom corner is compressed and becomes a mature ASB with shear deformation.

However, it might be another situation for the much wider sandwich structure, such as the structure composed of primary bifurcations in the middle of the shear region (see Fig. 9). Though, under the compressive stress and shear stress, the distances between parallel narrow ASB-bifurcations are reduced, but some of them might remain large even after stress collapse, which are possible to serve as favorable positions for nucleation of cracks due to the incongruity of deformation.

Moreover, attributing to the specific geometry of the hat-shaped specimen, the formation of ASBs will be dominated by the designed angle between the slip plane and the longitudinal axis, which may be different from the classical 45° for cylindrical samples [42,55]. Accordingly, the slip systems following the Schmid's law will be activated, contributing to the formation of a wide band from two or several narrow bands. It is recommended that the pure and simple shear mechanisms [56] and the interfacial absorption−desorption− transmission [57] should be considered in the future characterization and analysis of the aforementioned structure evolutions.

5 Conclusions

(1) According to force−displacement curve, plastic deformation of hat-shaped specimen can be divided into three stages named strain hardening, softening and shear localization. Each stage corresponds to different deformation mechanisms: Stage I (twining deformation), corresponding to obvious strain hardening stage; Stage II (initiation of ASB), corresponding to mildly decreasing stage in strain−stress curve; Stage III (shear localization), corresponding to mature stage of ASB.

(2) Microstructure fragmentation is the dominant mechanism for the α-Ti grain refinement in the shear region of Ti−6Al−2Zr−1Mo−1V alloy. Such sub-structure is attributed to dislocation walls and piled-up dislocation at twinning boundaries.

(3) The sandwich structure is composed of two narrow ASBs and one severely strained region. This microstructural evolution is due to geometrical relationship between imposed force and its shear direction. With further deformation, the sandwich structure keeps compressed and finally transfers to mature ASB when the distance between component narrow ASBs is small, whereas it is possible to serve as the nucleation sites of cracks when the distance is large.

References

[1] ZENER C, HOLLOMON J H. Effect of strain rate upon plastic flow of steel [J]. Journal of Applied Physics, 1944, 15(1): 22−32.
[2] XU Y B, ZHANG J H, BAI Y L, MEYERS M A. Shear localization in dynamic deformation: Microstructural evolution [J]. Metallurgical and Materials Transactions A, 2008, 39(4): 811.
[3] WALLEY S M. Shear localization: A historical overview [J]. Metallurgical and Materials Transactions A, 2007, 38(11): 2629−2654.
[4] TIMOTHY S P. The structure of adiabatic shear bands in metals: A critical review [J]. Acta Metallurgica, 1987, 35(2): 301−306.
[5] MARCHAND A, DUFFY J. An experimental study of the formation process of adiabatic shear bands in a structural steel [J]. Journal of the Mechanics and Physics of Solids, 1988, 36(3): 251−283.
[6] MEYERS M A, SUBHASH G, KAD B K, PRASAD L. Evolution of microstructure and shear-band formation in α-hcp titanium [J]. Mechanics of Materials, 1994, 17(2): 175−193.
[7] DODD B, BAI Y. Width of adiabatic shear bands [J]. Materials Science and Technology, 1985, 1(1): 38−40.
[8] GRADY D E. Properties of an adiabatic shear-band process zone [J]. Journal of the Mechanics and Physics of Solids, 1992, 40(6): 1197−1215.
[9] OUYANG S H, LIU B, LIU Y, ZAN X, LIANG X P, LI Z. Dynamic tensile behavior of PM Ti−47Al−2Nb−2Cr−0.2W intermetallics at elevated temperatures [J]. Transactions of Nonferrous Metals Society of China, 2019, 29(6): 1252−1262.
[10] TAO Z J, FAN X G, YANG H, MA J, LI H. A modified Johnson–Cook model for NC warm bending of large diameter thin-walled Ti−6Al−4V tube in wide ranges of strain rates and temperatures [J]. Transactions of Nonferrous Metals Society of China, 2018, 28(2): 298−308.
[11] GUO Y Z, RUAN Q C, ZHU S X, WEI Q, CHEN H S, LU J, HU B, WU X H, LI Y L, FANG D N. Temperature rise associated with adiabatic shear band: Causality clarified [J]. Physical Review Letters, 2019, 122(1): 015503.
[12] HUANG B, MIAO X F, LUO X, YANG Y Q, ZHANG Y M. Microstructure and texture evolution near the adiabatic shear band (ASB) in TC17 titanium alloy with starting equiaxed microstructure studied by EBSD [J]. Materials Characterization, 2019, 151: 151−165.
[13] ZHU S X, GUO Y Z, RUAN Q C, CHEN H S, LI Y L, FANG D N. Formation of adiabatic shear band within Ti−6Al−4V: An in-situ study with high-speed photography

and temperature measurement [J]. International Journal of Mechanical Sciences, 2020, 171: 105401.

[14] MEYERS M A, XU Y B, XUE Q, PÉREZ-PRADO M T, MCNELLEY T R. Microstructural evolution in adiabatic shear localization in stainless steel [J]. Acta Materialia, 2003, 51(5): 1307−1325.

[15] XU Y B, MEYERS M A. Deformation, phase transformation and recrystallization in the shear bands induced by high-strain rate loading in titanium and its alloys [J]. Journal of Materials Science & Technology, 2006, 22(6): 737−746.

[16] NESTERENKO V F, MEYERS M A, LASALVIA J C, BONDAR M P, CHEN Y J, LUKYANOV Y L. Shear localization and recrystallization in high-strain, high-strain-rate deformation of tantalum [J]. Materials Science and Engineering A, 1997, 229: 23−41.

[17] HINES J A, VECCHIO K S, AHZI S. A model for microstructure evolution in adiabatic shear bands [J]. Metallurgical and Materials Transactions A, 1998, 29(1): 191−203.

[18] CHICHILI D R, RAMESH K T, HEMKER K J. The high-strain-rate response of alpha-titanium: Experiments, deformation mechanisms and modeling [J]. Acta Materialia, 1998, 46(3): 1025−1043.

[19] YANG D K, CIZEK P, HODGSON P D, WEN C E. Microstructure evolution and nanograin formation during shear localization in cold-rolled titanium[J]. Acta Materialia, 2010, 58(13): 4536−4548.

[20] SHAHAN A R, TAHERI A K. Adiabatic shear bands in titanium and titanium alloys: A critical review [J]. Materials & Design, 1993, 14(4): 243−250.

[21] ME-BAR Y, SHECHTMAN D. On the adiabatic shear of Ti−6Al−4V ballistic targets [J]. Materials Science and Engineering A, 1983, 58: 181−188.

[22] GREBE H A, PAK H R, MEYERS M A. Adiabatic shear localization in titanium and Ti−6pctAl−4pctV alloy [J]. Metallurgical Transactions A, 1985, 16(5): 761−775.

[23] SUN K, YU X D, TAN C W, MA H L, WANG F C, CAI H N. Effect of microstructure on adiabatic shear band bifurcation in Ti−6Al−4V alloys under ballistic impact [J]. Materials Science and Engineering A, 2014, 595: 247−256.

[24] ZHOU T F, WU J J, CHE J T, WANG Y, WANG X B. Dynamic shear characteristics of titanium alloy Ti−6Al−4V at large strain rates by the split Hopkinson pressure bar test [J]. International Journal of Impact Engineering, 2017, 109: 167−177.

[25] LEE W S, LIN C F. Plastic deformation and fracture behaviour of Ti−6Al−4V alloy loaded with high strain rate under various temperatures [J]. Materials Science and Engineering A, 1998, 241(1): 48−59.

[26] GAO P F, QIN G, WANG X X, LI Y X, ZHAN M, LI G J, LI J S. Dependence of mechanical properties on the microstructural parameters of TA15 titanium alloy with tri-modal microstructure [J]. Materials Science and Engineering A, 2019, 739: 203−213.

[27] LIU L M, DU X, ZHU M L, CHEN G Q. Research on the microstructure and properties of weld repairs in TA15 titanium alloy [J]. Materials Science and Engineering A, 2007, 445−446: 691−696.

[28] SUN Q J, XIE X. Microstructure and mechanical properties of TA15 alloy after thermo-mechanical processing [J]. Materials Science and Engineering A, 2018, 724: 493−501.

[29] ZHAO A M, YANG H, FAN X G, GAO P F, ZUO R, MENG M. The flow behavior and microstructure evolution during ($\alpha+\beta$) deformation of β wrought TA15 titanium alloy [J]. Materials & Design, 2016, 109: 112−122.

[30] ZHAO H J, WANG B Y, JU D Y, CHEN G J. Hot tensile deformation behavior and globularization mechanism of bimodal microstructured Ti−6Al−2Zr−1Mo−1V alloy [J]. Transactions of Nonferrous Metals Society of China, 2018, 28(12): 2449−2459.

[31] MEYERS M A, NESTERENKO V F, LASALVIA J C, XUE Q. Shear localization in dynamic deformation of materials: Microstructural evolution and self-organization [J]. Materials Science and Engineering A, 2001, 317: 204−225.

[32] NESTERENKO V F, MEYERS M A, WRIGHT T W. Self-organization in the initiation of adiabatic shear bands [J]. Acta Materialia, 1998, 46(1): 327−340.

[33] LONGÈRE P. Respective/combined roles of thermal softening and dynamic recrystallization in adiabatic shear banding initiation [J]. Mechanics of Materials, 2018, 117: 81−90.

[34] GUO Y Z, RUAN Q C, ZHU S X, WEI Q, LU J N, HU B, WU X H, LI Y L. Dynamic failure of titanium: Temperature rise and adiabatic shear band formation [J]. Journal of the Mechanics and Physics of Solids, 2020, 135: 103811.

[35] PEIRS J, VERLEYSEN P, DEGRIECK J, COGHE F. The use of hat-shaped specimens to study the high strain rate shear behaviour of Ti–6Al–4V [J]. International Journal of Impact Engineering, 2010, 37(6): 703−714.

[36] LONGÈRE P, DRAGON A. Dynamic vs. quasi-static shear failure of high strength metallic alloys: Experimental issues [J]. Mechanics of Materials, 2015, 80: 203−218.

[37] KUANG L J, CHEN Z Y, JIANG Y H, WANG Z M, WANG R K, LIU C M. Adiabatic shear behaviors in rolled and annealed pure titanium subjected to dynamic impact loading [J]. Materials Science and Engineering A, 2017, 685: 95−106.

[38] XUE Q, GRAY G T, HENRIE B L, MALOY S A, CHEN S R. Influence of shock prestraining on the formation of shear localization in 304 stainless steel [J]. Metallurgical and Materials Transactions A, 2005, 36(6): 1471−1486.

[39] BRONKHORST C A, CERRETA E K, XUE Q, MAUDLIN P J, MASON T A, GRAY G T. An experimental and numerical study of the localization behavior of tantalum and stainless steel [J]. International Journal of Plasticity, 2006, 22(7): 1304−1335.

[40] GUDURU P R, ROSAKIS A J, RAVICHANDRAN G. Dynamic shear bands: An investigation using high speed optical and infrared diagnostics [J]. Mechanics of Materials, 2001, 33(7): 371−402.

[41] TENG X, WIERZBICKI T, COUQUE H. On the transition from adiabatic shear banding to fracture [J]. Mechanics of Materials, 2007, 39(2): 107−125.

[42] PEIRS J, TIRRY W, AMIN-AHMADI B, COGHE F, VERLEYSEN P, RABET L, SCHRYVERS D, DEGRIECK J. Microstructure of adiabatic shear bands in Ti6Al4V [J]. Materials Characterization, 2013, 75: 79−92.

[43] FISCHER F D, REISNER G, WERNER E, TANAKA K, CAILLETAUD G, ANTRETTER T. A new view on transformation induced plasticity (TRIP) [J]. International Journal of Plasticity, 2000, 16(7): 723−748.

[44] FISCHER F D, SUN Q P, TANAKA K. Transformation-induced plasticity (TRIP) [J]. Applied Mechanics Reviews, 1996, 49(6): 317−364.

[45] SUN K, YU X D, TAN C W, MA H L, WANG F C, CAI H N. Influence of adiabatic shear bands intersection on the ballistic impact of Ti–6Al–4V alloys with three microstructures [J]. Materials Science and Engineering A, 2014, 606: 257−267.

[46] HINES J A, VECCHIO K S. Recrystallization kinetics within adiabatic shear bands [J]. Acta Materialia, 1997, 45(2): 635−649.

[47] YANG Y, WANG B F. Dynamic recrystallization in adiabatic shear band in α-titanium [J]. Materials Letters, 2006, 60(17): 2198−2202.

[48] LI Z Z, WANG B F, ZHAO S T, VALIEV R Z, VECCHIO K S, MEYERS M A. Dynamic deformation and failure of ultrafine-grained titanium[J]. Acta Materialia, 2017, 125: 210−218.

[49] MITCHELL A. MeltFlow-VAR [Z]. Plymouth, US: Innovative Research, LLC, 2007.

[50] JONES I P, HUTCHINSON W B. Stress-state dependence of slip in Ti−6Al−4V and other HCP metals [J]. Acta Metallurgica, 1981, 29(6): 951−968.

[51] KISHIDA K, KIM J G, NAGAE T, INUI H. Experimental evaluation of critical resolved shear stress for the first-order pyramidal $c + a$ slip in commercially pure Ti by micropillar compression method [J]. Acta Materialia, 2020, 196: 168−174.

[52] WILLIAMS J C, BAGGERLY R G, PATON N E. Deformation behavior of HCP Ti−Al alloy single crystals [J]. Metallurgical and Materials Transactions A, 2002, 33(13): 837−850.

[53] KIPP M E, GRADY D E. Dynamic fracture growth and interaction in one dimension [J]. Journal of the Mechanics and Physics of Solids, 1985, 33(4): 399−415.

[54] GRADY D E, KIPP M E. The growth of unstable thermoplastic shear with application to steady-wave shock compression in solids [J]. Journal of the Mechanics and Physics of Solids, 1987, 35(1): 95−119.

[55] RITTEL D, LANDAU P, VENKERT A. Dynamic recrystallization as a potential cause for adiabatic shear failure [J]. Physical Review Letters, 2008, 101(16): 165501.

[56] OGATA S, LI J, YIP S. Ideal pure shear strength of aluminum and copper [J]. Science, 2002, 298(5594): 807−811.

[57] MISHIN Y, ASTA M, LI J. Atomistic modeling of interfaces and their impact on microstructure and properties [J]. Acta Materialia, 2010, 58(4): 1117−1151.

近 α 型 Ti−6Al−2Zr−1Mo−1V 钛合金帽形试样在高应变速率下的剪切局部化行为

杜予晅 [1,2]，杨新亮 [2]，李祖树 [2]，郝 芳 [1,3]，毛友川 [1,3]，李少强 [1]，刘向宏 [1]，冯 勇 [1]，严志明 [2]

1. 西部超导材料科技股份有限公司，西安 710018；

2. WMG, University of Warwick, Coventry CV4 7AL, UK；

3. 西北工业大学 凝固技术国家重点实验室，西安 710072

摘 要：采用 Hopkinson 冲击实验装置(SHPB)研究近 α 型 Ti−6Al−2Zr−1Mo−1V 钛合金帽形试样剪切局部化的组织特征，通过背散射电子衍射技术(EBSD)揭示帽形试样的组织演变及剪切变形机制。结果表明，绝热剪切带的形核与扩展受几何因素及组织因素的影响。变形影响区中的位错增殖、组织细化和温升提供基本的组织条件。除位错滑移外，在剪切区中还发现了大量的拉伸孪生，孪晶界大大加速了组织细化过程。三明治结构对绝热剪切带最终形态有很大影响，在动态变形过程中，这种结构会形成更宽、更稳定的绝热剪切带。但是，很宽的三明治结构也可能成为利于裂纹形核的位置。

关键词：Ti−6Al−2Zr−1Mo−1V 合金；绝热剪切带；Hopkinson 冲击实验装置；帽形试样；三明治结构

(Edited by Wei-ping CHEN)